Surface modification of $NiCo_2Te_4$ nanoclusters: a highly efficient electrocatalyst for overall water-splitting in neutral solution

Leiming Tao [a, b], Min Huang [c], Shaojun Guo [d], Qinglong Wang [a], Man Li [a], Xin Xiao [a], Gengyu Cao [c], Yong Shao [e], Yan Shen [a,*], Yongqing Fu [f], Mingkui Wang [a]

[a] Wuhan National Laboratory for Optoelectronics, Huazhong University of Science and Technology, Luoyu Road 1037, Wuhan 430074, P. R. China

[b] School of Science, Guangdong University of Petrochemical Technology, Maoming, Guangdong 525000, P. R. China

[c] State Key Laboratory of Magnetic Resonance and Atomic and Molecular Physics, Wuhan Institute of Physics and Mathematics, Chinese Academy of Sciences, Wuhan 430071, P. R. China

[d] Department of Materials Science and Engineering, College of Engineering, Peking University, Beijing 100871, P. R. China

[e] Key Laboratory of the Ministry of Education for Advanced Catalysis Materials, Zhejiang Normal University, Jinhua 321004, P. R. China

[f] Faculty of Engineering and Environment, Northumbria University, Newcastle upon Tyne, NE1 8ST, UK

Corresponding author: ciac_sheny@mail.hust.edu.cn

ABSTRACT: In this paper, we for the first time report the boosting catalytic activity and durability of nickel cobaltite telluride ($NiCo_2Te_4$) nanocluster bifunctional catalysts by surface modification with perylene-tetracarboxylic-dianhydride for overall water-splitting in neutral solution. We reveal that tuning energy distribution of nanoclusters via a simple surface ligand can drastically increase the catalytic activity towards efficient hydrogen and oxygen evolution reaction simultaneously. A two-electrode based water electrolysis cell using this newly developed nanocluster catalyst operates at a low bias voltage of 1.55 V to achieve a current density of 10 $mA \cdot cm^{-2}$ in near-neutral pH solution for overall water-splitting. This, to the best of our knowledge, represents the most efficient Mixed-transition-metal (MTM)-based electrode that has so far been reported for electrochemical water splitting.

KEYWORDS: Nanocluster; $NiCo_2Te_4$; Water splitting; Electrocatalyst; Mixed-transition-metal

1. Introduction

Electrochemical water-splitting is one of the most promising methods to efficiently produce hydrogen (and oxygen) for generating clean and renewable energy. Since the first observation of water electrolysis by van Trostwijk and Deiman in 1789, many different types of electrolysis cells have been proposed and constructed to produce hydrogen, mainly including alkaline electrolyzer, polymer electrolyte membrane electrolyzer (acidic), and solid oxide electrolyse. [1] Different electrolyzers function in slightly different ways, mainly due to the different type of electrolyte material and catalyst involved. Several metal oxides or metal phosphides routinely used for water splitting typically run at very high (alkaline) or low (proton exchange membrane) pH, which makes them prone to corrosion. [2, 3] Consequently, there is a need to move away from the extreme pH regimes characteristic of such traditional commercial devices because such corrosive conditions limit the types of electrodes and cell components.[4] Therefore, it remains a great challenge to develop efficient, durable, and low-cost new-generation catalysts for electrochemical water-splitting reaction in neutral solution. Mixed-transition-metal (MTM)-based electrocatalysts have emerged as novel pH-universal electrocatalysts for water-splitting, owing to their desirable electrical conductivity, synergistic effect of bimetallic atoms, and structural stability. [5, 6] The hydrogen evolution reaction (HER) activities of MTM-based electrocatalysts, *e.g.*, Ni/Co-based phosphides/selenides/sulfides/ oxides (Ni-Co-A, A=P, Se, S, O), are highly dependent on the adsorption strength of hydrogen to the anions (A). For example, Yu *et al*. suggested that P substitution of anions (A) in the Ni-Co-A could modulate the electron configuration, lower the hydrogen adsorption energy, and facilitate the desorption of hydrogen on the active sites, resulting in superior HER catalytic activity in alkaline solution. [7] In this case the transition metal tellurides (TMT) materials have attracted increasing interest for applications in

electrochemical water splitting. The $CoTe_2$ possesses a low adsorption strength for H_2 and thus presents highly electro-catalytic activity toward the HER. [8] This works well with the $NiTe_2$ toward the HER, which shows a comparable activity (276 mV@10 $mA \cdot cm^{-2}$) to the $CoTe_2$ (246 mV@10 $mA \cdot cm^{-2}$) in acid solution. [8, 9] These good performances are obtained in acidic solutions. It is noticed that there are few bifunctional catalytic materials exhibiting outstanding HER/OER activities in neutral-pH electrolytes. For example, very recently the Janus nickel cobalt phosphide catalysts have demonstrated remarkable activity and stability in neutral-pH water splitting. [10]

Recently, nanometer-sized clusters (1-5 nm typically) have opened a doorway for new generation of highly efficient electrocatalysts with remarkable catalytic activity and selectivity. [11, 12] For example, the bimetallic $PtAu_{24}$ nanoclusters have showed excellent electrochemically catalytic activity for H_2 production in acidic solution. [11] This can be attributed to their large surface/volume ratio and tunable electronic structure when the surface properties are the major concern for catalysts. In this regard, a large percentage of atoms are on or near the surfaces for clusters in such a small size regime. Particularly, the existence of vast interface between nanoclusters and the surrounding medium plays a profound effect. However, for practical application the long-term stability of nanocluster-based catalysts generally needs to be improved significantly.[13] Furthermore, the catalytic performance of clusters may become worse significantly as decreasing their size presumably due to slow transport of carriers. Therefore, various strategies including surface ligand engineering have been proposed to solve above-mentioned issues. [10, 14] Indeed, some ligands can act as “poison”, limiting the accessibility of active sites as well as a “promoter”, resulting in an unpredicted activity and stability. [15-17] Currently, the surface ligands are only limited to small molecule ligands or graphene-molecule supporting layer systems. Therefore, it is urgent to develop new surface modifier with function of both ligand engineering and supporting layer for fine-tuning of nanocluster’s properties.

This study, for the first time, reports a new electrocatalysts based on nickel cobaltite telluride ($NiCo_2Te_4$) nanoclusters for highly efficient water-splitting reaction in neutral solution. The $NiCo_2Te_4$ nanoclusters decorated with perylene-3,4,9,10-tetracarboxylic dianhydride (PTCDA) can be efficiently synthesized *via* an organic phase reaction process. The planar PTCDA molecule, consisting of a perylene core and two anhydrides, possesses high carrier mobility and excellent chemical stability. [14] The newly designed catalyst of $NiCo_2Te_4$/PTCDA exhibited an overpotential of 60 mV at 10 $mA \cdot cm^{-2}$ and a turnover frequency of 20.9 s^{-1} at a potential of -100 mV (vs. RHE) during the HER electrocatalytic activity in near-neutral pH solution. Additionally, this catalyst showed a high catalytic activity towards OER with a low overpotential of 120 mV at 10 $mA \cdot cm^{-2}$. A current density of 10 $mA \cdot cm^{-2}$ can be easily achieved at an applied cell voltage of 1.55 V across the neutral pH solution electrolyzer when this bifunctional electrocatalyst is applied as both the anode and cathode simultaneously.

2. Experimental Section

Reagent clusters of $Co(acac)_3$ (1 mM), $Ni(acac)_3$ (0.5 mM), oleic acid (6 mM), oleylamine (6 mM), and benzyl ether (20 mL) were mixed and magnetically stirred inside a three-necked flask under a constant flow of nitrogen. The mixture was heated to 200 °C for 30 min and then 2 mL of TOP-Te at 1 M mixed with 4 mL of oleic acid was quickly injected inside at 275 °C under the protection of nitrogen gas. The mixture was heated at 265 °C for another 10 min. The obtained mixture with a black-brown color was cooled down to room temperature. Under ambient conditions, ethanol (40 mL) was added into the mixture, and a black precipitate was obtained and then separated via centrifugation. The black product was dispersed into the hexane in the presence of oleic acid (0.05 mL) and oleylamine (0.05 mL). Centrifugation (10,000 rpm for 10 min) was applied to remove any undispersed residues in the solution. The product of $NiCo_2Te_4$ clusters was then precipitated, centrifuged (10,000 rpm, 10 min) to remove the solvent, and re-dispersed into hexane. Under identical

conditions, reagents of $Co(acac)_3$ (1 mM) and $Ni(acac)_2$ (0.5 mM) with TOPSe, TOPS or TOPO were processed to fabricate $NiCo_2X_4$ (X=Se, S, O) clusters that could be readily dispersed into hexane, and finally a dark red-brown hexane suspension was obtained.

To synthesize $NiCo_2Te_4$/PTCDA, 40 mg of PTCDA was suspended in 20 mL of dichloromethane under a constant stirring at 30-35 °C, and then added into a 1 ml of 0.5 mM $NiCo_2Te_4$ clusters. [14] The ethanedioic acid was dissolved into the solution, which was stirred under the protection of nitrogen for 24 hours. The volume of the solution was then reduced by one-half under a nitrogen gas flow, and the solution was filtered to remove any soluble materials. The filtrate was treated with charcoal and evaporated to obtain the final product of 110 mg. A pure sample was given using recrystallization from ether.

Theoretical calculations were based on DFT and performed using a Vienna Ab initio simulation package (VASP) simulation package. [18] The exchange and correlation functions with a Perdew-Burke-Ernzerh of generalized gradient corrected approximation (GGA) [19] and projector-augmented wave (PAW) [20] pseudopotentials were used during the calculations. The wave function was described with a plane wave basis set and an energy cutoff of 400 eV was used. The PTCDA films were modeled with a slab supercell containing two PTCDA molecules. $NiCo_2Te_4$ clusters were put onto the PTCDA molecules at the site where two PTCDA were connected in various orientations to search for the most stable structures. The vacuum thickness was set to be 10.0 Å which separated the slabs. A single Γ point was used in sampling the Brillouin zone due to the numerical limitations. For accurately analyzing the interactions between PTCDA molecules and $NiCo_2Te_4$ clusters as well as the inter-PTCDA interactions, the van der Waals interactions were corrected using the vdW-D2 method. [21] The effective values of U (U_{eff}) for Co and Ni were chosen to be 6.42 eV and 6.31 eV, based on previous study and our test calculations. [22, 23]

3. Results and discussion

The $NiCo_2Te_4$ nanoclusters were firstly synthesized with high-temperature solution phase reaction according to previous reports. [15] The TEM characterization clearly illustrates that the obtained $NiCo_2Te_4$ clusters are about 1.98 nm in diameter with a narrow size distribution (Fig. 1A). The high-resolution TEM image in Fig. 1B reveals an inter-planar spacing of 0.28 nm assigning to the (011) planes of $NiCo_2Te_4$ nanoclusters. Fig. 1C shows the XRD patterns of as-synthesized $NiCo_2Te_4$ nanoclusters (curve 1) which are perfectly agreed with a cubic structured spinel (space group, FD-3m) with lattice constants of a=b=c=7.546 Å and lattice angles of α=β=γ=60.007° (figs. S1a and S1b). The diffraction peaks match with those of the $CoNiTe_2$ (JCPDS card No. 03-065-3377) and $NiTe_2$ (JCPDS card No. 03-065-3377). The energy-dispersive X-ray (EDX) spectrum characterization and the integrated atomic molar ratio further verify the composition of samples to be $NiCo_2Te_4$ (Fig. 1D). The unique elements distribution (Ni, Co, and Te) of $NiCo_2Te_4$ nanoclusters was further confirmed by EDX elemental mapping (Figs. 1E-1H).

Fig. 2A outlines the synthesis procedures of $NiCo_2Te_4$/ PTCDA nanoclusters through a ring opening reaction among $NiCo_2Te_4$ and planar PTCDA (figs. S1c and S1d) mixture in dichloromethane at 30-35 °C. [24-26] The diffraction peaks in the XRD patterns of the as-synthesized $NiCo_2Te_4$/PTCDA (Fig. 2B) at $2\theta > 30^o$ can be well-assigned to $NiCo_2Te_4$ while those less than 30^o correspond to the planar structured PTCDA (fig. S1e). The well-crystallized $NiCo_2Te_4$ nanoclusters are uniformly distributed onto the PTCDA platform (Fig. 2C and 2D). The binding $NiCo_2Te_4$ onto planar PTCDA was further experimentally verified by X-ray photoelectron spectroscopy (XPS) characterization. For the Te 3d spectrum of $NiCo_2Te_4$, the peaks at 572.3 eV and 582.6 eV correspond to Te^{2-} bonds of the Te $3d_{5/2}$ and Te $3d_{3/2}$. For the XPS Te3d spectrum of $NiCo_2Te_4$/ PTCDA, the newly appeared peaks at 576 eV and 586.4 eV are assigned to Te-O bonds (Fig. 2E). Fig. 2F shows the C 1s spectra of $NiCo_2Te_4$/PTCDA, $NiCo_2Te_4$, and PTCDA samples. The peaks at

288.8 eV and 290 eV are assigned to the O=C-O-C=O of cyclic anhydride from the PTCDA. There are seven main peaks, for example the peak at 771.4 eV for Co^{0}, the peaks at 782.7 eV and 796.7 eV for Co^{2+}, the peaks at 780.1 eV and 795 eV for Co^{3+}, and two peak satellite at 788.5 eV and 804.2 eV in the $NiCo_2Te_4$ cluster, respectively (Fig S3a). The density of Co^{2+} /Co^{3+} is 0.7 $NiCo_2Te_4$ cluster. There are six main peaks, corresponding to elemental Co^{3+} (the peaks at 779.7 eV and 795.8 eV), Co^{2+} (the peaks at 782 eV and 798.3 eV), and two peak satellite at 785.5 eV and 802.4 eV in the $NiCo_2Te_4$/PTCDA composite (Fig S3b). The density of Co^{2+} /Co^{3+} is 1.1 for the $NiCo_2Te_4$/PTCDA composite. As shown in Fig. S3a and S3b, the density of Co^{2+} /Co^{3+} is lower as compared the density of the $NiCo_2Te_4$ cluster with that of the $NiCo_2Te_4$/PTCDA. There are six main peaks for Ni in the $NiCo_2Te_4$ cluster, corresponding to elemental Ni^{2+} (at 854.4 eV and 872.4 eV), Ni^{3+} (at 856.0 eV and 874.0 eV), satellite peak at 861.1 eV and 879.1 eV, respectively (Fig S3c). With regarding to the elemnet of Ni, the binding energy values of Ni 2p XPS spectrum at 853.7 eV and 872.6 eV for $NiCo_2Te_4$ cluster (Fig. S3c) and $NiCo_2Te_4$/PTCDA (Fig. S3d) composite are assigned to the Ni $2p_{3/2}$ and Ni $2p_{1/2}$, corresponding to a Ni^{2+} oxidation state. The peak at 880.6 eV attributing to O-Ni bond is almost at the same position for those of $NiCo_2Te_4$/PTCDA and $NiCo_2Te_4$. A possible mechanism for the chemical binding of PTCDA could be firstly correlated with the opening ring step of anhydride terminal groups (O=C-O-C=O) followed by a formation of C-O-Te bond between the Te atom of $NiCo_2Te_4$ and the oxygen (O_α) atom of PTCDA (Fig. S2).

We computed the charge density difference of $NiCo_2Te_4$ and $NiCo_2Te_4$/PTCDA (e.g., $\Delta\rho = \rho_1-\rho_2-\rho_{PTCDA}$) before and after surface modification to explore the effect of chemical binding between the $NiCo_2Te_4$ and PTCDA molecules, where the ρ_1 and ρ_2 represent the charge densities of $NiCo_2Te_4$ clusters modification with and without PTCDA molecules, respectively, and ρ_{PTCDA} is the charge density of PTCDA molecules. Figs. S4a-4c present the simulation result of charge-displacement. The analysis on the Bader's charge shows that a number of 0.7 *e* transfers from the $NiCo_2Te_4$ to PTCDA once combining both of them together. As shown in Table S2,

the conduction band of PTCDA (-4.49 eV) is larger than the conduction band of $NiCo_2Te_4$ (-6.11 eV). The electron shall flow from $NiCo_2Te_4$, the one with higher Fermi level, to PTCDA, the one with lower Fermi level. In other words, in the composite of $NiCo_2Te_4$/PTCDA, the PTCDA possesses a higher charge density than the $NiCo_2Te_4$, which could induce a strong attraction between the $NiCo_2Te_4$ and PTCDA (possible through O_α-Te as discussed above). Our latest results, obtained using Fourier transform infrared (FT-IR) spectroscopy characterization, also confirmed the interaction between the PTCDA and $NiCo_2Te_4$ (Fig. S4d).

Fig. 3A presents the linear sweep voltammetry (LSV) curves for the $NiCo_2Te_4$/PTCDA electrode to characterize their HER activity in 1 M phosphate buffer solution (PBS, pH=7) recorded at a scan rate of 5 $mV \cdot s^{-1}$. The $NiCo_2Te_4$/PTCDA achieved a current density of 10 and 100 $mA \cdot cm^{-2}$ at an applied potential of 60 and 120 mV (vs. RHE), respectively. Under the same condition, the $NiCo_2Te_4$ or PTCDA electrode showed less electrocatalytic activity to the HER. Fig. 3B presents electrochemical surface area (ECSA)-corrected Tafel plots derived from Koutecky-Levivh plots for the $NiCo_2Te_4$/PTCDA and $NiCo_2Te_4$. A small Tafel slopes for the $NiCo_2Te_4$/PTCDA electrode (38 $mV \cdot dec^{-1}$) indicates its efficient HER electrocatalytic performance. This result further suggests that the HER on the $NiCo_2Te_4$/PTCDA proceeds through Volmer-Tafel mechanism and the H+H recombination step is rate limiting. [27] The activity metric of catalysts was further evaluated in terms of turn over frequency (TOF) according to Equation 1 [28] and the results are presented in the inset of Fig. 3B.

$$TOF = \frac{J \times A}{z \times F \times m} \qquad (1)$$

where J is the current density ($A \cdot cm^{-2}$) at an overpotential of 0.1 V, A being the electrochemical active surface area (ECSA), m being the mass of active materials (in mole), z being the number of the transferred electrons (z=2 for H_2 and z=4 for O_2), respectively. Clearly, the $NiCo_2Te_4$/PTCDA electrode has the highest value of TOF at 27.1 s^{-1}, which is about 4 times larger than that of $NiCo_2Te_4$ (6.5 s^{-1}). Fig. 2C

compares the Tafel plots and overpotential at 10 $mA \cdot cm^{-2}$ for various reported HER catalysts, verifying the good performance of $NiCo_2Te_4$/PTCDA. The Faraday efficiency (FE) of the $NiCo_2Te_4$/PTCDA electrode is nearly 100% for the HER in 1 M PBS medium based on the gas chromatography characterization results (fig. S5). Electrochemical impedance spectroscopy (EIS) measurement results further reveal that the $NiCo_2Te_4$/PTCDA electrode has a smaller polarization resistance than that of $NiCo_2Te_4$ (Fig. 3D). This indicates that the increased activity of $NiCo_2Te_4$/PTCDA can be probably attributed to the small charge transfer resistance. It also suggests the molecular PTCDA with large π-conjugation could enhance charge transport and catalytic kinetics of the $NiCo_2Te_4$ electrode. Fig. 3E presents that $NiCo_2Te_4$/PTCDA electrolyzer can retain a current density of 10 $mA \cdot cm^{-2}$ over 20 h of continuous operation without obvious degradation, while this current density decreased in case of $NiCo_2Te_4$. After tested with the continuous cyclic voltammetry characterization for 2,000 cycles at a scanning rate of 10 $mV \cdot s^{-1}$, the $NiCo_2Te_4$/PTCDA still exhibited a polarization curve with a stable overpotential of -60 mV at 10 $mA \cdot cm^{-2}$ (Fig. 3F).

Meanwhile, the $NiCo_2Te_4$/PTCDA electrode also showed good catalytic behaviors to the OER. In 1 M PBS the $NiCo_2Te_4$/PTCDA achieved low overpotentials of 120 and 240 mV at different current densities of 10 and 100 $mA \cdot cm^{-2}$ for the OER, with a Tafel slope of 50 mV per decade (Fig. 4A and 4B). The recorded overpotential for $NiCo_2Te_4$/ PTCDA was less than the $NiCo_2O_4$ electrode (150 mV at 10 mA cm^{-2}), however, the Tafel slope was higher than the $NiCo_2O_4$ electrode (30 mV dec^{-1} at 10 mA cm^{-2}). Fig. 4C compares the Tafel plots and overpotential at 10 $mA \cdot cm^{-2}$ for various reported OER catalysts, verifying the good performance of $NiCo_2Te_4$/PTCDA for the OER. Fig. 4D presents that for the case of $NiCo_2Te_4$/PTCDA electrode the current density retains over 20 h of continuous operation for OER without obvious degradation.

The catalysts were examined with XPS characterization after catalytic runs to investigate structural changes associated with the electrocatalysis. Fig. 4E presents the

Te 3d XPS spectrum of the fresh $NiCo_2Te_4$/PTCDA samples (curve 1) and that of after the HER testing (curve 2) and after the OER testing (curve 3). The Te 3d of the fresh $NiCo_2Te_4$ samples, after the HER testing and after the OER testing were shown curve 4-6 in Fig 4E, respectively. There are four main peaks, for example the peaks at 572.3 eV and 582.6 eV correspond to Te^{2-} bonds, and the peaks at 576 eV and 586.4 eV are assigned to Te-O_x, respectively (Fig. 4E). For the Te 3d spectrum of $NiCo_2Te_4$ (curve 4), the peaks at 572.3 eV and 582.6 eV correspond to Te^{2-} bonds of the Te $3d_{5/2}$ and Te $3d_{3/2}$. For the XPS Te3d spectrum of $NiCo_2Te_4$/ PTCDA (curve 1), the newly appeared peaks at 576 eV and 586.4 eV are assigned to Te-O bonds. The relative peak ratio (%) is a region integrated areas (P_1): all of the integral areas (ΣP_x) measured. The relative peak ratio (Te^{2-}) are 0.65(curve 1), 0.68 (curve 2), 0.63(curve 3), 0.90(curve 4), 0.8 (curve 5) and 0.1(curve 6), respectively. The relative peak ratio (Te-O_x) are 0.35(curve 1), 0.32(curve 2), 0.37(curve 3), 0.1(curve 4), 0.2 (curve 5) and 0.9(curve 6), respectively. Clearly, the Te 3d XPS spectrum kept almost identical for the $NiCo_2Te_4$/PTCDA sample before and after electrochemical measurements. However, the XPS peaks for the $NiCo_2Te_4$ significantly changed after electrochemical testing (see curves 4, 5, and 6). This result demonstrates the function of the molecular PTCDA to protect Te from oxidization. There is not obvious for Co and Ni in $NiCo_2Te_4$ cluster and $NiCo_2Te_4$/PTCDA composite.

Density functional theory (DFT) calculation was carried out on the free energy for the possible adsorption of intermediates H^* (O^*) on various positions within the $NiCo_2Te_4$/ PTCDA catalyst during the HER process. The DFT result in fig. S6a verifies the effective contribution of ligands (i.e., PTCDA) to the adsorption of intermediates. In this case, the smallest value of adsorption energy for H^* (O^*) on the obtuse angle position principally suggests the point for an easy desorption of intermediates. Furthermore, we found the adsorption energies for these intermediates on the PTCDA at positions of obtuse angle and the terminal of PTCDA are lower than those of $NiCo_2Te_4$ (fig. S6b). The adsorption of reaction intermediates onto the catalysts surface plays critical role on the bond-breaking and bond-forming during the

catalytic processes. Frontier molecular orbital theory can provide a good understanding of key steps involved in these surface catalytic reactions. The strength of adsorption and bonding of reactants on catalyst surfaces are closely linked to the symmetry and spin states of reactant's molecular or atomic orbitals, which are dependent on the matching between the energy levels of reactants and those of catalyst's surfaces. [29] For example, when the electron Fermi energy equals that potential of the reactions in equilibrium (the ΔG equals zero), the chemical reaction will produce easily. These plus potentials are called the thermodynamic reduction potential η_H and oxidization potential η_O of the catalyst. A good catalytic performance would be expected for the case with a high overlapping of the density of states (DOS) of catalysts with that of water molecules. Fig. 5A shows the calculated DOS profiles of $NiCo_2Te_4$/PTCDA, $NiCo_2Te_4$, Pt, PTCDA and H_2O molecules across the Fermi level with DFT simulation employing the Gerischer-Marcus model. [30] Clearly, the DOS patterns present an overlapping (indicated by a pink dotted circuit) between the oxidation and reduction potentials of the water molecules and that of Pt serving as an efficient catalyst toward electrochemical hydrogen production. Though the individual $NiCo_2Te_4$ (red line) or PTCDA (green line) has less electron distribution in this range, the energy levels of valence band and conduction band of $NiCo_2Te_4$ are shifted by modifying with PTCDA toward the levels of H_2O/O_2 and H_2/H_2O equivalent electrochemical potentials, respectively. This indicates surface engineering of $NiCo_2Te_4$ with PTCDA can significantly tune the composites' energy levels.

We further synthesized several typical nanocluster-based catalysts including NiO, Co_3O_4, $NiCo_2O_4$, $NiCo_2S_4$, and $NiCo_2Se_4$ through controlling particle size but without surface modification with PCTDA and systematically evaluated their catalytic behaviors. [30, 31] Fig. 5B illustrates the band diagram of Pt, $NiCo_2Te_4$/PTCDA, $NiCo_2Te_4$, $NiCo_2Se_4$, $NiCo_2S_4$, $NiCo_2O_4$, Co_3O_4, NiO, and PTCDA. The valence band positions of NiO (2.71 V) [32], Co_3O_4 (2.61 V) [33], $NiCo_2O_4$ (2.34 V) [34], $NiCo_2S_4$ (2.17 V) [35], $NiCo_2Se_4$ (1.77 V) and $NiCo_2Te_4$ (1.61 V) are approaching the potential of water-splitting. The $NiCo_2Te_4$ possesses a valence band position nearer to the

potential of water-splitting among $NiCo_2X_4$ (X=O, S, Se, Te) (Table S2). After modifying with PTCDA, its ($NiCo_2Te_4$/PTCDA) valence band position (1.18 V) and conduction band position (-0.02 V) were further tuned toward the levels of H_2O/O_2 and H_2/H_2O potentials, respectively (Fig. 5B).

Many reactions proceed with rates that are orders of magnitude larger at a surface than in the gas or liquid phase. For reactions with more than one possible product the presence of a surface can completely change the selectivity. The adsorption of reaction intermediates onto the catalysts surface plays critical role on the bond-breaking and bond-forming during the catalytic processes. It is well-known that HER process in alkaline medium is governed by the dissociation of water molecules, where two intermediate species forms, i.e., O^- and H^+ which needs to adsorb and desorb on catalyst surface with variable deriving energies to complete the reaction [36-40]. In the particular case of hydrogen evolution, it turns out that these general principles can be quantified by analysing the free energy of hydrogen adsorption ΔG_H; this quantity is a reasonable descriptor of hydrogen evolution activity for a wide variety of metals and alloys. They adopted the approach of using calculated values of ΔG_H that the closer ΔG_H is to zero, the new HER catalysts is the better catalyst. Fig. 6A compares the adsorption free energy (ΔG_H) for hydrogen on these samples. The PTCDA has a larger ΔG_H value (~6.5 eV) than others, mainly due to the anhydride terminal groups (O=C-O-C=O) and its weak 2D planar π-conjugation structure. As mentioned earlier, a strong ionic interaction (O_α-Te) between the $NiCo_2Te_4$ and PTCDA would decrease electronegativity of the $NiCo_2Te_4$ and reduce the ΔG_H between the $NiCo_2Te_4$ and PTCDA, respectively. Therefore, atomic hydrogen can be easily released from the $NiCo_2Te_4$/PTCDA surface compared to others (Fig. 6A), which significantly enhances their catalytic activities during water-splitting. [41] Fig. 6B and Table S1 summarize the overpotentials (the error range being about 2 mV) of these samples ($NiCo_2Te_4$/PTCDA, $NiCo_2O_4$, $NiCo_2S_4$, $NiCo_2Se_4$, $NiCo_2Te_4$, NiO, Co_3O_4 and Pt) at 10, 20, and 100 $mA \cdot cm^{-2}$ for the HER and the OER in 1 M PBS solution. Interestingly, all the compounds containing Co showed better HER

performance than those of Ni-based counterparts. The integration of Ni and Co into the MTM electrocatalysts further improves their catalytical performance. This further verifies the MTM-based materials emerging as efficient electrocatalysts for water splitting. [5, 6] The $NiCo_2O_4$, $NiCo_2S_4$, $NiCo_2Se_4$ and $NiCo_2Te_4$ have overpotentials of 330, 214, 142, and 80 mV at a current density of 10 $mA \cdot cm^{-2}$ for the HER (Table S1), respectively. This behavior follows the electronegativity of the elements of O (3.44), S (2.58), Se (2.55), and Te (2.1) in the $NiCo_2$-based compounds.

We further fabricated two-electrode ($NiCo_2Te_4$/PTCDA ||$NiCo_2Te_4$/PTCDA) electrolysis cells using Nafion membrane as separator for efficient overall water-splitting. The $NiCo_2Te_4$/PTCDA cell merely required bias voltages of 1.55, 1.61, and 1.78 V to reach current densities of 10, 20, and 100 $mA \cdot cm^{-2}$ in the PBS solution (pH=7) (Fig. 4F). A current density of 10 $mA \cdot cm^{-2}$ can be obtained at a cell voltage of 1.55 V, representing an overpotential of 220 mV for overall water-splitting. The overpotential value is superior to most of previously reported electrocatalysts (Table S3), including the noble metal-based Pt/C||RuO_2 cell (green, 380 mV at 10 $mA \cdot cm^{-2}$), FeB_2 (340 mV at 10 $mA \cdot cm^{-2}$) [42], CoP (390 mV at 10 $mA \cdot cm^{-2}$) [43], Co_3Se_4 (360 mV at 10 $mA \cdot cm^{-2}$) [44]. The inset of Fig. 4F shows the stability of water splitting by the electrolysis cells ($NiCo_2Te_4$/PTCDA||$NiCo_2Te_4$/PTCDA) at a voltage of 1.61 V, producing gas bubbles of hydrogen and oxygen based on the gas chromatography characterization results (fig. S4). The $NiCo_2Te_4$/PTCDA cells exhibited an excellent stability for 30 hours of long-term water electrolysis without obvious degradation when tested at a constant potential of 1.61 V (Fig. 4F and the inset).

4. Conclusion

In summary, this work presents the nanocluster catalysts for efficient overall water-splitting application. The newly designed catalyst of $NiCo_2Te_4$/PTCDA exhibited an overpotential of 60 mV at 10 $mA \cdot cm^{-2}$ and a turnover frequency of 20.9 s^{-1} during the HER electrocatalytic activity in near-neutral pH solution. Additionally,

this catalyst showed a high catalytic activity towards OER with a low overpotential of 120 mV at 10 $mA \cdot cm^{-2}$. A two-electrode water electrolysis cell using the $NiCo_2Te_4$/PTCDA only needed a low bias voltage of 1.55 V to acquire a current density of 10 $mA \cdot cm^{-2}$ for overall water-splitting. This is remarkably superior to those reported electrochemical activities of the transition metal catalysts. The excellent electrocatalytic activities of $NiCo_2Te_4$/PTCDA could be attributed to the enhanced charge transport, antioxidant properties and the perfect tuning of the energy distributions of valence electrons of $NiCo_2Te_4$ induced by surface ligand PTCDA.

Supporting Information. Experimental sections; XRD data of $NiCo_2Te_4$; XPS of $NiCo_2Te_4$/PTCDA; theoretical calculation results; Comparison of the HER and the OER performance for catalysts.

ACKNOWLEDGMENT

The authors gratefully acknowledge financial support from the NSFC Major International (Regional) Joint Research Project NSFC-SNSF (51661135023), NSFC (21673091), the Fundamental Research Funds for the Central Universities (HUST: 2016YXMS031, 2018KFYXKJC034), the Director Fund of the WNLO, and the Open Funds of the State Key Laboratory of Electroanalytical Chemistry (SKLEAC201607), UK Engineering and Physical Sciences Research Council (EPSRC) EP/P018998/1, a Newton Mobility Grant (IE161019) from the UK Royal Society and the National Natural Science Foundation of China, and Royal Academy of Engineering UK-Research Exchange with China and India.

REFERENCES

[1] Q. Xu, H. Jiang, H. Zhang, Y. Hu, C. Li, *Appl. Catal., B*, 242 (2019) 60-66.
[2] Y. Ma, C. Wu, X. Feng, H. Tan, L. Yan, Y. Liu, Z. Kang, E. Wang, Y. Li, *Energy Environ. Sci.*, 10 (2017) 788-798.
[3] S. Dutta, A. Indra, Y. Feng, H. Han, T. Song, *Appl. Catal., B*, 241 (2019) 521-527.
[4] Z. Kou, L. Zhang, Y. Ma, X. Liu, W. Zang, J. Zhang, S. Huang, Y. Du, A.K. Cheetham, J. Wang, *Appl. Catal., B*, 243 (2019) 678-685.
[5] R. Zhang, X. Wang, S. Yu, T. Wen, X. Zhu, F. Yang, X. Sun, X. Wang, W. Hu, *Adv. Mater.*, 29 (2017) 1605502.
[6] T. Tang, W. Jiang, S. Niu, N. Liu, H. Luo, Y. Chen, S. Jin, F. Gao, L. Wan, J. Hu, *J. Am. Chem. Soc.*, 139 (2017) 8320-8328.
[7] Z. Fang, L. Peng, Y. Qian, X. Zhang, Y. Xie, J.J. Cha, G. Yu, *J. Am. Chem. Soc.*, 140 (2018) 5241-5247.
[8] T. Lu, C. Chen, M. Basu, C. Ma, R. Liu, *Chem. Commun.*, 51 (2015) 17012-17015.
[9] K. Wang, Z. Ye, C. Liu, D. Xi, C. Zhou, Z. Shi, H. Xia, G. Liu, G. Qiao, *ACS Appl. Mater. Interfaces*, 8 (2016) 2910-2916.
[10] R. Wu, B. Xiao, Q. Gao, Y. Zheng, X. Zheng, J. Zhu, M. Gao, S. Yu, *Angew. Chem., Int. Ed.*, 130 (2018) 15671-15675.
[11] Y. Ge, S. Gao, P. Dong, R. Baines, P.M. Ajayan, M. Ye, J. Shen, *Nanoscale*, 9 (2017) 5538-5544.
[12] K. Kwak, W. Choi, Q. Tang, M. Kim, Y. Lee, D. Jiang, D. Lee, *Nat. Commun.*, 8 (2017) 14723.
[13] J. Xu, T. Liu, J. Li, B. Li, Y. Liu, B. Zhang, D. Xiong, I. Amorim, W. Li, L. Liu, *Energy Environ. Sci.*, 11 (2018) 1819-1827.
[14] K. Li, Y. Li, Y. Wang, J. Ge, C. Liu, W. Xing, *Energy Environ. Sci.*, 11 (2018) 1232-1239.
[15] L. Cao, Y. Wang, T. Chen, W. Zhang, X. Yu, K. Ibrahim, J. Wang, H. Qian, F. Xu, D. Qi, A.T.S. Wee, *J. Chem. Phys.*, 135 (2011) 174701.
[16] J.R. Edman, H.E. Simmons, *J. Org. Chem.*, 33 (1968) 3808-3816.
[17] Y. Zou, L. Kilian, A. Schöll, T. Schmidt, R. Fink, E. Umbach, *Surf. Sci.*, 600 (2006) 1240-1251.
[18] G. Kresse, J. Furthmüller, *Phys. Rev. B*, 54 (1996) 11169-11186.
[19] J.P. Perdew, K. Burke, M. Ernzerhof, *Phys. Rev. Lett.*, 77 (1996) 3865-3868.
[20] G. Kresse, D. Joubert, *Phys. Rev. B*, 59 (1999) 1758-1775.
[21] S. Grimme, J. *Comput. Chem.*, 27 (2006) 1787-1799.
[22] J. He, S.Y. Ma, P. Zhou, C.X. Zhang, C. He, L.Z. Sun, *J. Phys. Chem. C*, 116 (2012) 26313-26321.
[23] J. He, P. Zhou, N. Jiao, S.Y. Ma, K.W. Zhang, R.Z. Wang, L.Z. Sun, *Sci. Rep.*, 4 (2014) 4014.
[24] J.R. Edman, H.E. Simmons, *J. Org. Chem.*, 33 (1968) 3808-3816.

[25] Y. Zou, L. Kilian, A. Scholl, T. Schmidt, R. Fink, E. Umbach, *Surf. Sci.*, 600 (2006) 1240-1251.
[26] G. Gavrila, D.R.T. Zahn, W. Braun, *Appl. Phys. Lett.*, 89 (2006) 162102.
[27] B.E. Conway, B.V. Tilak, *Electrochim. Acta*, 47 (2002) 3571-3594.
[28] M. Gong, Y. Li, H. Wang, Y. Liang, J.Z. Wu, J. Zhou, J. Wang, T. Regier, F. Wei, H. Dai, *J. Am. Chem. Soc.*, 135 (2013) 8452-8455.
[29] A.J. Bard, L.R. Faulkner, Electrochemical Methods: Fundamentals and Applications, 2nd edn, *J. Chem. Educ.*, 60 (2001) 80–89.
[30] M.T. Greiner, M.G. Helander, W. Tang, Z. Wang, J. Qiu, Z. Lu, *Nat. Mater.*, 11 (2011) 76.
[31] C. M. Chuang, P.R. Brown, V. Bulović, M.G. Bawendi, *Nat. Mater.*, 13 (2014) 796.
[32] Y. Miseki, H. Kato, A. Kudo, *Energy Environ. Sci.*, 2 (2009) 306.
[33] H. Zhang, S. Pokhrel, Z. Ji, H. Meng, X. Wang, S. Lin, C.H. Chang, L. Li, R. Li, B. Sun, M. Wang, Y. Liao, R. Liu, T. Xia, L. Mädler, A.E. Nel, *J. Am. Chem. Soc.*, 136 (2014) 6406-6420.
[34] K. Dileep, B. Loukya, P. Silwal, A. Gupta, R. Datta, *J. Phys. D: Appl. Phys.*, 47 (2014) 405001.
[35] C. Xia, P. Li, A.N. Gandi, U. Schwingenschlögl, H.N. Alshareef, *Chem. Mater.*, 27 (2015) 6482-6485.
[36] J.K. Nørskov, T. Bligaard, A. Logadottir, J.R. Kitchin, J.G. Chen, S. Pandelov, U. Stimming, *J. Electrochem. Soc.*, 152 (2005) J23-J26.
[37] J. Rossmeisl, A. Logadottir, J.K. Nørskov, *Chem. Phys.*, 319 (2005) 178-184.
[38] J. Greeley, T.F. Jaramillo, J. Bonde, I. Chorkendorff, J.K. Nørskov, *Mater. Sustain. Energy*, pp. 280-284.
[39] J. Rossmeisl, Z.W. Qu, H. Zhu, G.J. Kroes, J.K. Nørskov, *J. Electroanal. Chem.*, 607 (2007) 83-89.
[40] I.C. Man, H. Su, F. Calle-Vallejo, H.A. Hansen, J.I. Martínez, N.G. Inoglu, J. Kitchin, T.F. Jaramillo, J.K. Nørskov, J. Rossmeisl, *ChemCatChem*, 3 (2011) 1159-1165.
[41] E. Yoo, T. Okata, T. Akita, M. Kohyama, J. Nakamura, I. Honma, *Nano Lett.*, 9 (2009) 2255-2259.
[42] H. Li, P. Wen, Q. Li, C.C. Dun, J.H. Xing, C. Lu, S. Adhikari, L. Jiang, D.L. Carroll, S.M. Geyer, *Adv. Energy Mater.*, 7 (2017) 1700513-n/a.
[43] Y.P. Zhu, Y.P. Liu, T.Z. Ren, Z.Y. Yuan, Adv. Funct. Mater., 25 (2015) 7337-7347.
[44] W. Li, X.F. Gao, D.H. Xiong, F. Wei, W.G. Song, J.Y. Xu, L.F. Liu, Adv. *Energy Mater.*, 7 (2017) 1602579-n/a.

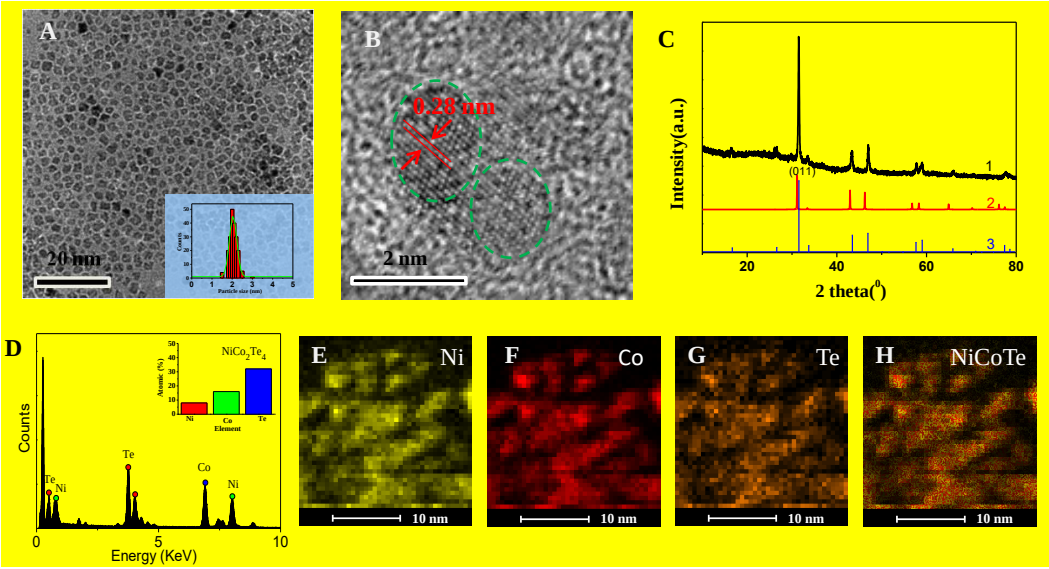

Figure 1. (A) Transmission electron microscope (TEM) image, (B) HR-TEM, (C) X-ray diffraction patterns of as-synthesized-$NiCo_2Te_4$ (curve 1), $CoNiTe_2$ (curve 2), $NiTe_2$ (curve 3), (D) TEM-EDX spectrum of as-synthesized-$NiCo_2Te_4$. The inset shows the clusters integrated atomic molar ration distribution. (E-G) EDX elemental mapping of Ni, Co, Te, and (H) the composed RGB image obtained by superposing the three elemental maps for the sample of $NiCo_2Te_4$.

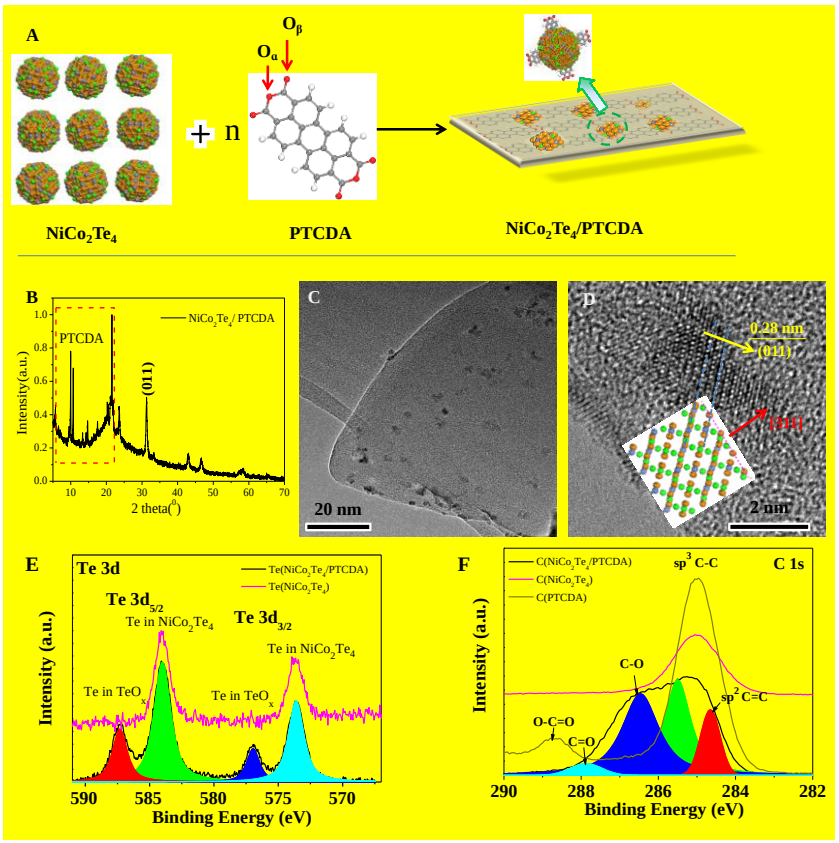

Figure 2. (A) Schematic illustrations for synthesis of $NiCo_2Te_4$/PTCDA (abbreviation of nickel cobaltite telluride clusters modified with perylene-3,4,9,10-tetracarboxylic dianhydrid). The O_α and O_β represent O atoms at cyclic anhydride and carbonyl of PTCDA, respectively. (B) X-ray diffraction, (C) TEM images, and (D) HR-TEM of $NiCo_2Te_4$/PTCDA. The inset shows the model of $NiCo_2Te_4$ (011). (E) and (F) XPS spectra of Te 3d and C 1s for $NiCo_2Te_4$/PTCDA and $NiCo_2Te_4$ samples.

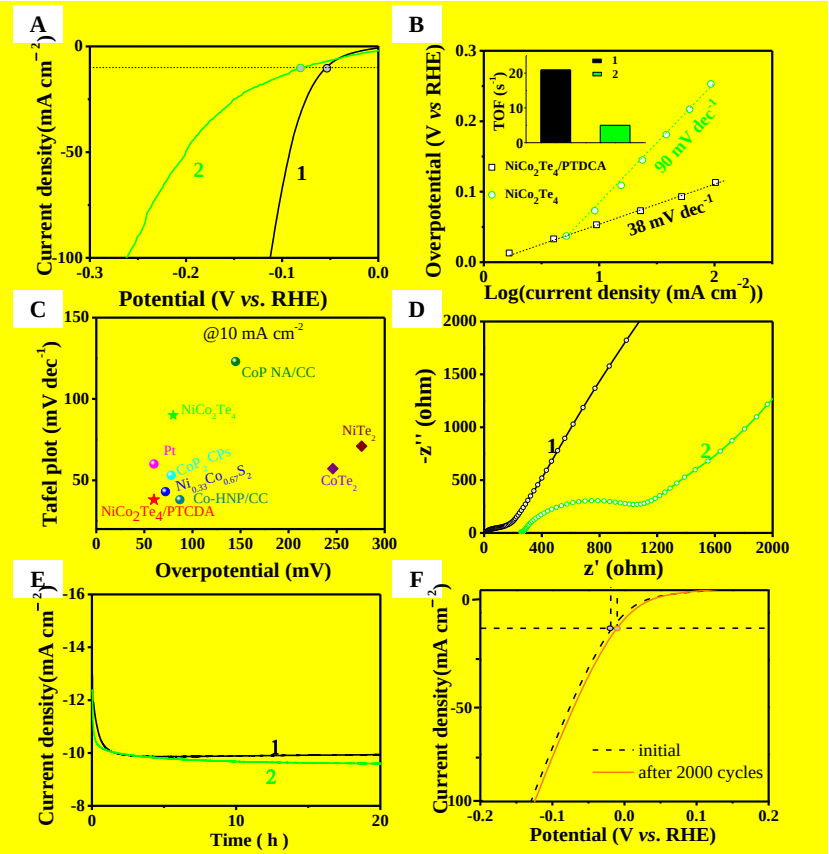

Figure 3. (A) Linear sweep polarization curves obtained in 1 M PBS (pH=7) for the $NiCo_2Te_4$/PTCDA (curve 1), $NiCo_2Te_4$ (curve 2). (B) The ECSA-corrected Tafel plots derived from Koutecky-Levivh plots. The inset shows ECSA corrected turnover frequency (TOF) of $NiCo_2Te_4$, and $NiCo_2Te_4$/PTDCA at a potential of -100 mV for HER in 1 M PBS. (C) The Tafel slope versus overpotential at 10 mA·cm^{-2} for various reported HER catalysts. Values were list in Table S1. (D) Nyquist plots of $NiCo_2Te_4$/PTCDA (curve 1) and $NiCo_2Te_4$ (curve 2) from 10 kHz to 0.1 Hz at -0.2 V vs. RHE. (E) Chronoamperometric response recorded from $NiCo_2Te_4$/PTCDA (curve 1) and $NiCo_2Te_4$ (curve 2) at the constant overpotentil to reach current density of -10 mA·cm^{-2} for HER. (F) The HER curves initial and after (curve 2) 2000 cycles with a scan rate of 100 mV·s^{-1} between 0.20 and -0.20 V. All electrochemical tests are conducted in 1 M PBS electrolyte.

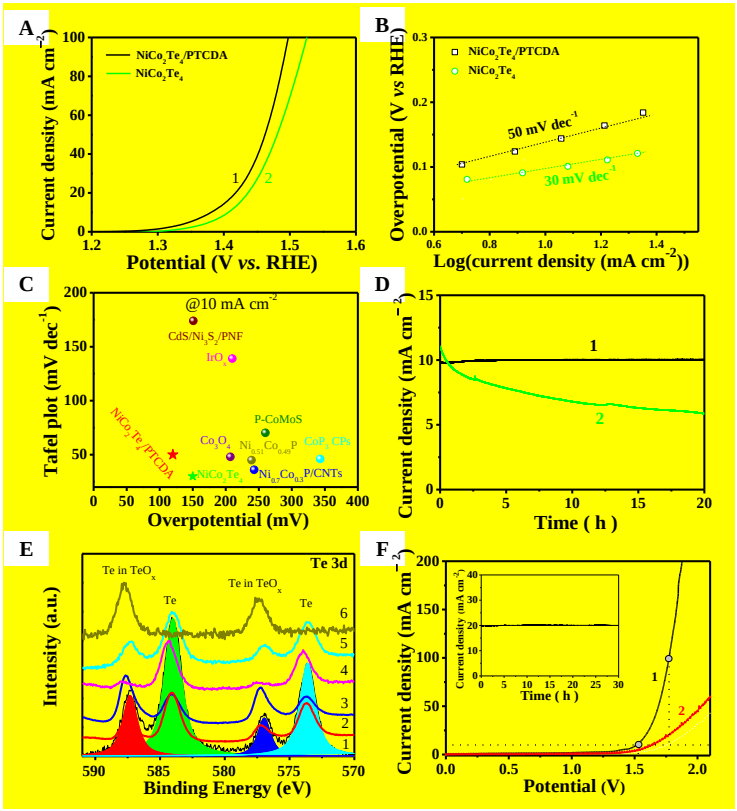

Figure 4. (A) Linear sweep polarization curves for the $NiCo_2Te_4$/PTCDA. (B) The ECSA-corrected Tafel plots derived from Koutecky-Levivh plots. (C) Tafel slope versus overpotential at 10 mA·cm^{-2} for various reported OER catalysts. Values were list in Table S1. (D) Chronoamperometric response recorded from the $NiCo_2Te_4$/PTCDA (curve 1) and $NiCo_2Te_4$ (curve 2) at the constant overpotentil to reach current density of 10 mA·cm^{-2} for OER. (E) XPS spectra of Te 3d for the fresh $NiCo_2Te_4$/PTCDA electrode (curve 1), after HER testing (curve 2), after OER testing (curve 3), the fresh $NiCo_2Te_4$ electrode (curve 4), after HER testing (curve 5), after OER testing (curve 6). (F) Electrolyzer properties of $NiCo_2Te_4$/PTCDA||$NiCo_2Te_4$/PTCDA (curve 1). The inset shows the chronoampermetric curve of the $NiCo_2Te_4$/ PTCDA||$NiCo_2Te_4$/PTCDA electrolyzer at a static potential of 1.61 V for 30 hours. All electrochemical tests are conducted in 1 M PBS electrolyte.

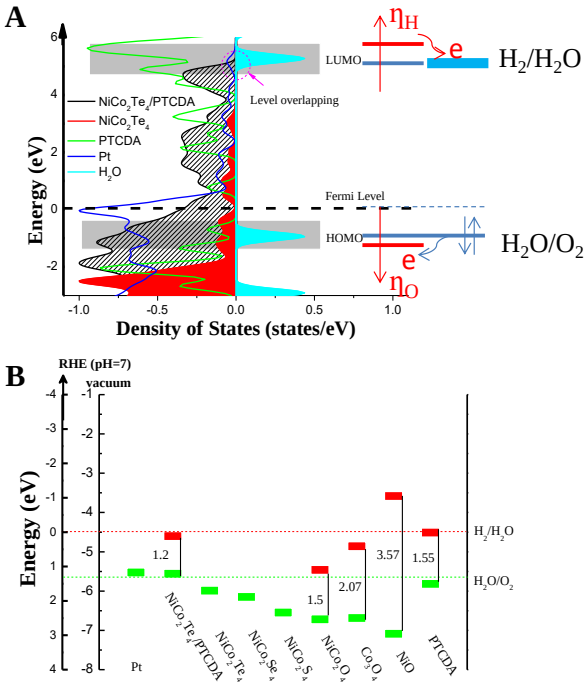

Figure 5. (A) The calculated density of states (DOS) of $NiCo_2Te_4$/PTCDA (black), $NiCo_2Te_4$ (red), PTCDA (green), Pt (blue), and H_2O (cyan); (B) Bandgap energy, Valence band and Conduction band positions of several samples on an energy scale (eV) vs. RHE/Vacuum level.

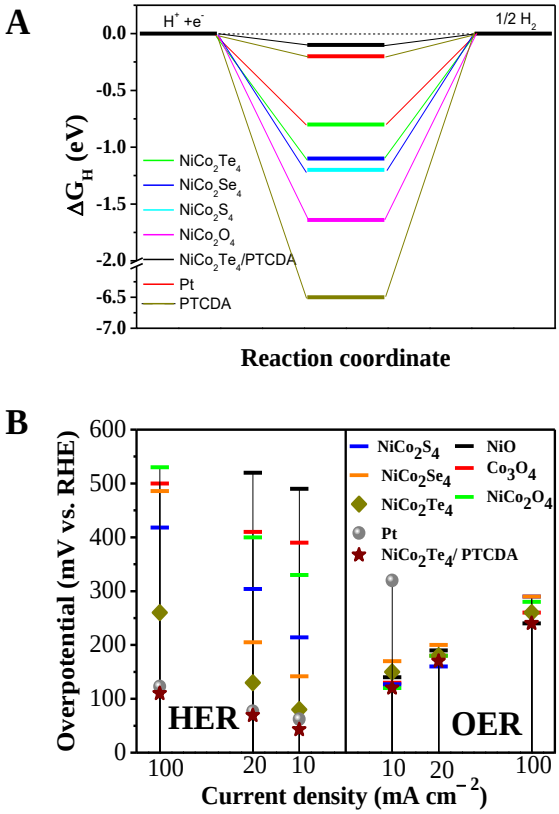

Figure 6. (A) Hydrogen adsorption free energy ΔG_H diagrams; (B) Performance of catalysts (2 nm clusters of NiO, Co_3O_4, $NiCo_2O_4$, $NiCo_2S_4$, $NiCo_2Se_4$, $NiCo_2Te_4$, $NiCo_2Te_4$/PTCDA, and Pt) for HER and OER. The overpotentials obtained at 10, 20, and 100 $mA \cdot cm^{-2}$ on various catalysts in 1 M PBS.